

RKHS-BA: A Semantic Correspondence-Free Multi-View Registration Framework with Global Tracking

Ray Zhang, Jingwei Song, Xiang Gao, Junzhe Wu, Tianyi Liu, Jinyuan Zhang, Ryan Eustice, Maani Ghaffari

Abstract—This work reports a novel Bundle Adjustment (BA) formulation using a Reproducing Kernel Hilbert Space (RKHS) representation called RKHS-BA. The proposed formulation is correspondence-free, enables the BA to use RGB-D/LiDAR and semantic labels in the optimization directly, and provides a generalization for the photometric loss function commonly used in direct methods. RKHS-BA can incorporate appearance and semantic labels within a continuous spatial-semantic functional representation that does not require optimization via image pyramids. We demonstrate its applications in sliding-window odometry and global LiDAR mapping, which show highly robust performance in extremely challenging scenes and the best trade-off of generalization and accuracy.

I. INTRODUCTION

Bundle Adjustment (BA) is widely used in visual perception algorithms such as Simultaneous Localization and Mapping (SLAM) and 3D Reconstruction. It jointly optimizes visual structures and all the camera parameters to construct a spatially-consistent 3D world model [73]. Existing BA methods include feature-based methods [73] and direct methods [26, 40, 52], and both are formulated as robust non-linear optimization problems.

Feature-based methods require extractions of sparse geometric representations, including points, lines, and planes, which are usually invariant to illumination noise or rotations [17, 18, 36, 50]. Then, in the optimization step, they minimize reprojected geometric residuals for features observed across multiple frames via multi-view geometry [36, 73]. The construction of such reprojected residuals naturally leads to sparse Hessian structures but relies on correct feature correspondences across multiple frames. Many works have been devoted to improving their robustness, such as improving frontend feature matching’s quality with deep networks [33], adopting robust loss functions [73], or probabilistically modeling data association hypothesis in the backend [20, 22, 53]. However, in highly texture-less or semi-static environments, feature association contaminated with outliers is still an open problem [56].

Direct or photometric-based methods take denser representations from images, such as the edges [24], surfaces [82, 92], or the raw pixel values [52], and then optimize the photometric loss under the assumption of brightness constancy [24, 62]. With the capability of adjusting the projective association during optimization [24], photometric BA demonstrates more

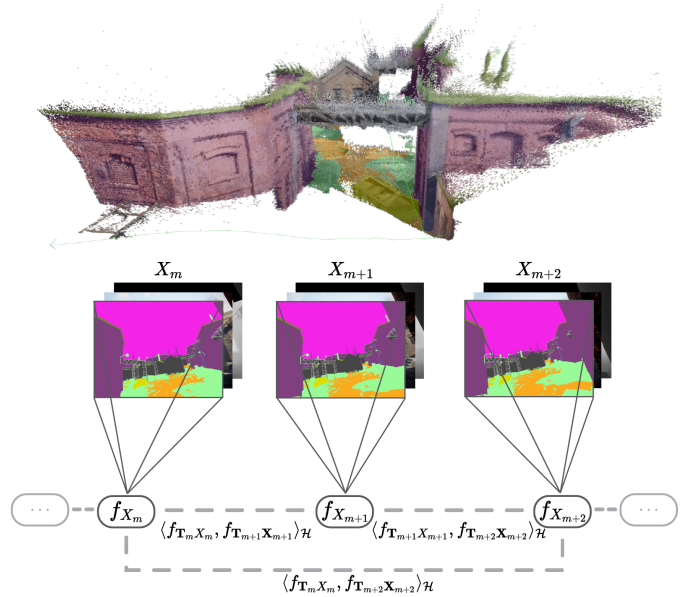


Fig. 1: We represent a point cloud observation as a function in the Reproducing Kernel Hilbert Space (RKHS), denoted as f_{X_m} , where X_m is the raw sensor measurements containing both geometric information like 3D points and non-geometric information such as color, intensity, and semantics. An inner product $\langle f_{T_m X_m}, f_{T_n X_n} \rangle_{\mathcal{H}}$ measures the alignment of two functions at timestamp m and n . The full objective function consisting of multiple frames is formulated as the sum of all inner products between all pairs of relevant frames.

robustness in environments with fewer textures or more repetitive patterns. However, full images need to be stored in the pose graph even in semi-dense approaches [95]. Furthermore, their illumination invariance presumption is seriously violated in outdoor situations where complex illumination, changeable weather, and dynamic objects exist.

Rich semantic information from modern vision sensors can contribute to the robustness of BA in such challenging scenarios. Specifically, we denote various types of visual information, including pixel classes, object instances, intensities, or colors, which are invariant to pose changes, as *hierarchical semantics*. For example, dense SLAM systems such as ElasticFusion and BAD-SLAM incorporate color consistency residuals as invariant visual information in their backend optimization [62, 81]. Object detection neural networks can provide another type of semantic information, that is, 2D or 3D object proposals from image streams [32, 72]. They enable the representation of object-level entities in the factor graph for feature-based systems [23, 54, 60]. Suma++ [11] leverages point-level dense semantics in LiDAR SLAM, where point-wise semantic similarity contributes to the residual weighting.

Preprint. Work in Progress.

R. Zhang, J. Song, X. Gao, J. Wu, T. Liu, J. Zhang, R. Eustice, and M. Ghaffari are with the University of Michigan, Ann Arbor, MI 48109, USA. {rzh, jingweso, gxian, junzhewu, tannert1, jyzh, eustice, maanigg} @umich.edu

In the paper, we report a novel direct BA framework with semi-dense hierarchical semantic representation in a Reproducible Kernel Hilbert Space (RKHS) (shown in Fig. 1). The proposed RKHS-BA constructs a specialized pose graph. Its nodes represent continuous functional representations. Its edges represent the corresponding frames’ geometric and hierarchical semantic alignment. Inspired by [91], we relax the strict data correspondence in previous BA methods by associating each point observation of one frame to multiple semantically similar points in other frames. The soft association naturally arises from a functional representation in some RKHS and constrains the geometric distance and the visual similarity when a new frame is observed. The optimization stage approximates the formulation with an Iteratively Reweighted Least Square (IRLS) solver.

In particular, this work has the following contributions.

1. A novel correspondence-free multi-view BA framework with hierarchical semantics in an RKHS representation called RKHS-BA.
2. We propose a new backend formulation of the pose graph that does not rely on strict data correspondence and encodes hierarchical semantic information in optimization.
3. A novel way to initialize the rotation globally of two-frame registration by searching for the minimum distance in RKHS over the Icosahedral symmetry as a discretization [94] of $SO(3)$.
4. We validate the proposed RKHS-BA with point cloud registration and odometry baselines on multiple synthetic and real-world datasets, including Stanford 3D Scanning Dataset [75], SemanticKITTI Dataset [5], and TartanAir Dataset [79].
5. We provide an open-source C++ implementation, which will be released after the paper decision.

Differences from CVO [12, 91] While sharing the same formulation for the alignment objective as the original CVO, RKHS-BA has three major improvements: a) The original CVO relies on a good enough initial guess because it directly performs gradient ascent. Instead, the proposed method leverages the distance measure in RKHS to evaluate a finite number of rotations uniformly spanning $SO(3)$ and thus supports global rotation registration. b) RKHS-BA extends the registration of two frames to a multi-frame scenario so that it can be applied in areas other than frame-to-frame odometry. For example, in SLAM, pose graphs consisting of multiple frames are often preferred over two frames because of the extra covisibility information [51]. In practical applications, CVO can be used to initialize the poses of RKHS-BA. c) First-order gradient-based methods uses more iterations than second-order optimization methods, and this will take even more time when densely-connected frame graphs of more frames are involved in the computation. The approximation of IRLS has finite weights even at large residuals and does not need techniques like truncated least squares [4].

II. RELATED WORKS

A. Registration of Multiple Point Sets

Point sets registration in direct methods estimates the poses of two or more point clouds in order to build a single and consistent model [38, 62, 81]. Repeatedly applying frame-to-frame pairwise registration leads to graduate accumulation of drifts because spatial consistency at nearby but non-adjacent frames is not considered. To reduce odometry drifts, some works perform model-to-frame registration, which fuses several latest point clouds into a local map with previous pose estimations, then registers the latest frame with the map [80, 81]. Model-to-frame registration requires accurate localization in earlier frames; otherwise, it risks yielding an inconsistent map as the registering source.

On the other hand, jointly estimating the poses of multiple point clouds can evenly distribute the errors and demonstrate accurate registration results in real datasets, but it requires the Expectation-Maximization (EM) procedure to infer data correspondence across multiple frames [16, 34, 46, 77]. RKHS-BA registers multiple frames simultaneously, which extends the benefits of RKHS representation to the backend optimization. In this formulation, the associations are not inferred but based on the pairwise similarity in the geometric distance and the semantic similarity.

B. Photometric Bundle Adjustment

Direct BA methods take wrapped photometric residuals from a large number of image pixels [24, 25, 52, 81]. Keyframe-based direct methods [25, 40, 62] usually construct residuals by projecting one frame’s intensity image to another. Map-centric methods [15, 52, 81] project the map elements onto the image pixels and establish the photometric loss. To improve robustness against outliers, robust estimators like T-distribution [6] and Huber-loss functions are wrapped around intensity residuals [26, 40].

A class of hybrid methods still uses dense or semi-dense points without relying on photometric losses. For example, SVO [29] performs feature alignment after dense tracking and converts the problem into classical feature-based solvers. Voldor [47] models the dense optical flow residual distribution with an empirical Fisk residual model.

RKHS-BA is a semi-dense bundle adjustment method that does not completely rely on intensity consistency or geometric residuals alone but is extendable to other hierarchical semantic measurements like pixel semantics or image gradients into the cost function. In addition, the representations of frames are not raw images [52], surfels [62] or flows [47], but continuous functions constructed from semi-dense point clouds.

C. Classical and Semantic Data Association

Data association is the process of registering features observed in different frames. It builds the topology of the factor graph and is heavily discussed in community [10]. Existing featured-based backend solvers like g2o [35] and iSAM2 [39] assume known data association hypotheses from the frontends. These hypotheses can come from the matching of invariant

visual feature points [45, 58] with methods like optical flow tracking [61] or stereo feature matching [36, 65]. In comparison, direct backends usually adopt projective data association. Keyframe-based direct methods [25, 26] project the points onto other frames’ epipolar lines and search for the pixel groups with the minimum intensity. Map-centric methods [81] project the map elements onto the image pixels and establish the correspondence. They differ from feature-based systems in the ability to adjust associations during optimization.

To improve backends’ robustness against wrong data association hypotheses, we can treat the associations themselves as latent variables [9]. One strategy is adding weights as additional variables to the potential data association hypothesis and optimizing both the poses and the weights [2, 67]. Another approach is the use of Non-Gaussian mixture models, for example, max-mixtures, to model multiple uncertain data association hypotheses [20, 21, 53], and can be solved by methods like nonparametric Bayesian belief propagation [30] or Dirichlet process [49, 90].

RKHS-BA is free from strict pixel-wise matching because each pixel’s correlation with other point clouds is *queried* from their function representations instead of finding a concrete point match. A point is matched to all the nearby points in the other frames whose appearance (in the form of semantic representation) is similar. Moreover, similar to direct methods, RKHS-BA enables soft data association during the BA optimization process.

D. Learning-based Bundle Adjustment

Recent works introduce deep neural networks’ predictions into the bundle adjustments of multiple frames. One class of works aims at utilizing accurate monocular depth estimations and pixel associations from neural networks and then performing classical or differentiable BA. CNN-SLAM [69] generates depth from CNN and then relies on a photometric-residual-based classical non-differentiable BA to optimize the poses. DVSO [86], TANDEM [41] and D3VO [87] uses Monocular deep depth networks to initialize the stereo disparity values. The loss function of the odometry includes the reprojected pixel difference residuals(self-supervised). Besides initialization, the depth map estimated from BA is further projected back to the right image to generate a disparity map and compare it with the network’s disparity prediction, as another loss term. BA-Net [68] make the BA process differentiable, when steps like damping factor be predicted. RAFT [70] and DROID-SLAM [71] use RNN to predict dense flow matches and then use a supervised dense photometric BA.

Another class of learning-based BA methods uses implicit neural embeddings as frame representations instead of predicting depth and pixel matches directly. CodeSLAM [8] and DeepFactors [14] use a deep compact code that encodes geometric information of each keyframe image. The depth can be inferred from the encoding and the intensity image with linear combinations of codes from multiple frames. The poses and the code are optimized together. iMap [66] provides a real-time implicit map representation via MLP. The network

is initialized randomly. To train the MLP with depth, for every pixel iMap queries along the ray in discrete depths and compare it with the network’s predictions. The resulting depth prediction is a weighted sum of depth value predictions along the ray. NeRF-SLAM [57] uses NeRF as the scene representation and is able to generate photorealistic maps.

E. LiDAR Bundle Adjustment

Unlike camera sensors, LiDAR observations have significantly finer depth measurements but are natively sparse, thus strict point-wise correspondence might not exist. Point-to-plane ICP [48] and GICP [63] choose a specific geometric entity, planes, centered at each point and minimize the point to the closest-associated plane’s Euclidean or Mahanobis distances. The point-to-plane distance loss can be extended to multi-frame local bundle adjustment algorithms for better odometry. For instance, LOAM [89] minimizes both point-to-plane and point-to-line distances. The associations of points to planes and lines are computed via geometric distances. LegoLOAM [64] improves association from 3D distance to 2D LiDAR range images. Suma further tries surfel maps and projective association. MULLS [55] further proposes using more different types of hand-crafted feature points, including information of linear, vertex, and planar points. Its tracking part uses data association with feature points and the loss functions consist of point-to-point, point-to-plane, and point-to-line distances.

Global LiDAR bundle adjustment adds the loop closure constraint to the procedure. Unlike pose graph optimization (PGO) which only considers the pose data’s consistency, the LiDAR bundle adjustment tries to optimize the full global map consistency of all the frames simultaneously. GICP Cost Factor [42] group all the frames into 10-20 sub-maps, each contained in voxels for fast query during data association. The full costs include the submap overlap loss and a loop closure pose loss. BALM [44] constructs the map consisting of adaptively-sized voxels of features, such as edges and planes. The loss function contains the point-to-plane and point-to-edge distances. The original point-to-plane minimization problem is transformed into the minimization of the eigenvalue of points covariance in each voxel. HBA [43] uses a hierarchical sub-mapping strategy to boost the running efficiency of BALM. CT-ICP [19] proposes a loop closure procedure aggregating point clouds projected onto an 2D elevation image.

F. RKHS Registration and Kernel Correlation

Continuous Visual Odometry (CVO) [31] proposes a new point cloud registration method that represents colored point clouds as continuous functions in RKHS and then aligns the two functions with gradient ascent. The step size during the optimization is approximated with a fourth-order Taylor expansion. Kernel correlation [74] is a special case of CVO that only performs geometric registration and optimizes the loss with a first-order approximation. SemanticCVO [91] extends CVO to tightly couple semantic information such as color or semantics with geometric information. RKHS-BA generalizes

SemanticCVO to a multi-frame formulation with a new IRLS solver and maintains the unified geometric-semantic model.

III. PROBLEM SETUP AND NOTATIONS

We denote the sequential K frames' robot poses as $\mathcal{T} = \{\mathbf{T}_1, \mathbf{T}_2, \dots, \mathbf{T}_K\}$ ($\mathbf{T}_I \in \text{SE}(3)$) and sensor observations $\mathcal{X} = \{X_1, X_2, \dots, X_K\}$ at each timestamp. Each sensor observation contains a finite collection of homogeneous points, $X_m = \{\mathbf{x}_1^m, \mathbf{x}_2^m, \dots\}$ ($\mathbf{x}_i^m \in \mathbb{R}^3$). Let \mathcal{C} be the set of covisible [51] frame pairs, such that each frame pair shares some partial view of the global model. The multi-view registration process identifies the transformations that jointly align all the sensor observations into a globally consistent model. Given some distance measure d in the point clouds' representation space, it can be formulated as follows:

$$\mathcal{T}^* = \arg \min_{\mathcal{T}} \sum_{(m,n) \in \mathcal{C}} d(\mathbf{T}_m X_m, \mathbf{T}_n X_n) \quad (1)$$

A. Review of SemanticCVO

In addition to the geometric information, every point \mathbf{x}_i^m might contain pose-invariant visual information of *various* dimensions, such as color, intensity, or pixel class labels. How to integrate these different types of visual information into the registration? SemanticCVO [91] proposes using continuous functions in a reproducing kernel Hilbert space (RKHS) to represent color and semantic point clouds, and then perform the two-frame registration in the function space. We provide a brief review here, and the readers can refer to its technical report to more details.

Let (V_1, V_2, \dots) be different inner product spaces describing different types of non-geometric features of a point, such as color, intensity, and semantics. To combine these features of different dimensions into a unified hierarchical semantic representation $\ell_{\mathcal{X}} : \mathcal{X} \rightarrow \mathcal{I}$ that is transformation-invariant, we use their tensor product, $V_1 \otimes V_2 \otimes \dots$, which also lies in an inner product space $(\mathcal{I}, \langle \cdot, \cdot \rangle_{\mathcal{I}})$. For example, for any $\mathbf{x}_i^m \in X_m$ with a 3-dimensional color feature $v_1 \in V_1$ and a 10-dimensional semantic feature $v_2 \in V_2$, its hierarchical semantic feature is $\ell_{\mathcal{X}}(\mathbf{x}_i^m) = v_1 \otimes v_2 \in V_1 \otimes V_2$.

SemanticCVO represents the point cloud observations X_m at frame m into a function $f_{X_m} : \mathbb{R}^3 \rightarrow \mathcal{I}$ living in a RKHS $f_{X_m} \in (\mathcal{H}, \langle \cdot, \cdot \rangle_{\mathcal{H}})$. The transformation \mathbf{T}_m at the corresponding timestamp m , $\text{SE}(3) \curvearrowright \mathbb{R}^3$ induces an action $\text{SE}(3) \curvearrowright \mathcal{H}$ by $\mathbf{T}_m f(X_m) := f_{\mathbf{T}_m X_m}$, representing the point cloud function under the transformation. With the kernel trick the point clouds are:

$$f_{\mathbf{T}X}(\cdot) := \sum_{\mathbf{x}_i \in X} \ell_X(\mathbf{x}_i) k(\cdot, \mathbf{T}\mathbf{x}_i), \quad (2)$$

where $\ell_X(\mathbf{x}_i)$ encodes the semantic information that does not vary with respect to robot poses. $k(\cdot, \mathbf{x}_i)$ encodes the geometric information that varies with robot poses.

The distance between two functions in the Hilbert space is

$$\begin{aligned} d(f_{X_m}, f_{\mathbf{T}X_n}) &= \|f_{X_m} - f_{\mathbf{T}X_n}\|_{\mathcal{H}}^2 \\ &= \langle f_{X_m}, f_{X_m} \rangle + \langle X_n, X_n \rangle - 2\langle f_{X_m}, f_{\mathbf{T}X_n} \rangle. \end{aligned} \quad (3)$$

while only the last term, the inner product of two functions, is relevant to the pose regression. The inner product of f_{X_m} and $f_{\mathbf{T}X_n}$ can be computed as

$$\begin{aligned} \langle f_{X_m}, f_{\mathbf{T}X_n} \rangle_{\mathcal{H}} &= \sum_{\substack{\mathbf{x}_i^m \in X_m \\ \mathbf{z}_j^n \in X_n}} \langle \ell_X(\mathbf{x}_i^m), \ell_X(\mathbf{z}_j^n) \rangle \cdot k(\mathbf{x}_i^m, \mathbf{T}_n \mathbf{z}_j^n) \\ &:= \sum_{\mathbf{x}_i^m \in X_m, \mathbf{z}_j^n \in X_n} c_{ij} \cdot k(\mathbf{x}_i^m, \mathbf{T}_n \mathbf{z}_j^n). \end{aligned} \quad (4)$$

This inner product between the two functions above is a double sum of all pairs of points from the two point clouds. Eq.(4) can be interpreted as a point-wise *soft data association* function, which considers both the geometry and the semantics. If the current estimates of the poses change during an iterative optimization, the association will reflect the change accordingly. If the semantic information is not used, the alignment of two geometric point clouds reduces to Kernel Correlation [74]. The two-frame case can be solved locally by gradient ascent given a good initial guess [12].

B. Generalized Multi-view Registration in RKHS

In BA problems, we are also interested in a joint pose optimization of multiple frames besides the original two-frame registration in SemanticCVO [91]. For example, Fig. 1 illustrates a pose graph of three frames. We now propose the full objective function over the entire pose graph as

$$F(\mathcal{T}) := \sum_{(m,n) \in \mathcal{C}} \underbrace{\langle f_{\mathbf{T}_m X_m}, f_{\mathbf{T}_n X_n} \rangle_{\mathcal{H}}}_{F^{mn}} \quad (5)$$

$$\mathcal{T}^* = \arg \max_{\mathcal{T}} F(\mathcal{T}), \quad (6)$$

Based on the above definition, the generalized objective function of RKHS-based bundle adjustment becomes

$$\begin{aligned} F(\mathcal{T}) &:= \sum_{(m,n) \in \mathcal{C}} \sum_{\mathbf{x}_i^m \in X_m, \mathbf{z}_j^n \in X_n} \underbrace{k(\mathbf{T}_m \mathbf{x}_i^m, \mathbf{T}_n \mathbf{z}_j^n) \cdot c_{ij}^{mn}}_{F_{ij}^{mn}} \\ \mathcal{T}^* &= \arg \max_{\mathcal{T}} F(\mathcal{T}). \end{aligned} \quad (7)$$

The objective function in Eq. (7) describes the full geometric and hierarchical semantic relationship for all the edges in the pose graph. Each c_{ij}^{mn} is invariant to the relative transformation; thus, it will be a constant during optimization. In practice, the double sum in (4) is sparse because a point $\mathbf{x}_i \in X$ is far away from the majority of the points $\mathbf{z}_j \in Z$, either in the spatial (geometry) space or one of the feature (semantic) spaces. The sparsity is dependent on the feature space differences.

IV. GLOBAL TWO-FRAME ROTATION INITIALIZATION

The objective function for in Eq.(7) is highly non-convex because it has the form as the sum of the exponentials, as well as the pose parameters on the $SO(3)$ manifold. In the two-frame situation, the original CVO [12, 31] work performs pose optimization with gradient ascent, which assumes a good initial guess that is not far away from the ground truth. However, there are no immediate initial guesses in real applications such as loop closure registrations and robot relocalizations.

To mitigate the issue of local minima, we can leverage the observation that Eq. (3) is a *continuous* distance measure between the input point cloud functions in the Hilbert space with respect to the poses. The key idea is that we can discretize the $SO(3)$ group into a finite number of rotations uniformly distributed on the manifold. Then, we are able to measure the quality of each initial pose guess by evaluating the distance measure. As the distance measure is continuous, the rotation demonstrating the minimum distance value is designated as the initial rotation.

We uniformly sample the space of $SO(3)$ based on the Icosahedral symmetry [13, 94]. As a convex polyhedron, it has 12 vertices, 30 edges, and 20 faces. We can construct 60 pre-computed rotational symmetries out of it. Specifically, this can be interpreted as the collection of all possible rotations that move each vertex of the polyhedron to the position of another vertex, while preserving the overall shape and structure of the polyhedron unchanged [94]. We evaluate the distance measure in with Eq. (3) the 60 different angles, then choose the one with the minimum distance value as our initial pose guess.

V. SEMANTICALLY INFORMED ITERATIVELY REWEIGHTED LEAST SQUARES BACKEND

In this section, we present a solver for the non-convex objective function of the multi-frame BA in Eq. (7). Given our proposed way of finding initial pose guesses in Sec. IV, we can obtain frame-to-frame odometry with gradient ascent as SemanticCVO [91]. However, for a large-scale BA problem consisting of thousands of frames and perhaps millions of residuals, first-order methods might not be efficient enough. Instead, we approximate the problem with Iteratively Weighted Least Squares (IRLS).

A. From RKHS to IRLS

For the kernel of our RKHS, \mathcal{H} , we choose the squared exponential kernel $k : \mathbb{R}^3 \times \mathbb{R}^3 \rightarrow \mathbb{R}$:

$$k(\mathbf{x}, \mathbf{z}) = \sigma^2 \exp\left(\frac{-\|\mathbf{x} - \mathbf{z}\|_3^2}{2\ell^2}\right), \quad (8)$$

for some fixed real parameters (hyperparameters) σ and ℓ (the *lengthscale*), and $\|\cdot\|_3$ is the standard Euclidean norm on \mathbb{R}^3 . With a good initialization of the frame poses $\mathcal{T} = \{\mathbf{T}_1, \dots, \mathbf{T}_K\}$ from tracking, and let $d(\mathbf{x}, \mathbf{z}) := \mathbf{x} - \mathbf{z}$, we can

expand each term F_{ij}^{mn} in (5)

$$\begin{aligned} F_{ij}^{mn} &= k(\mathbf{T}_m \mathbf{x}_i^m, \mathbf{T}_n \mathbf{z}_j^n) \cdot c_{ij}^{mn} \\ &= c_{ij}^{mn} \sigma^2 \exp\left(\frac{-\|\mathbf{T}_m \mathbf{x}_i^m - \mathbf{T}_n \mathbf{z}_j^n\|_3^2}{2\ell^2}\right) \\ &:= c_{ij}^{mn} k(d(\mathbf{T}_m \mathbf{x}_i^m, \mathbf{T}_n \mathbf{z}_j^n)^2) \end{aligned} \quad (9)$$

If we apply a perturbation $\epsilon_m \in \mathbb{R}^6$ on the right of \mathbf{T}_m as

$$\mathbf{T}_m^* = \mathbf{T}_m \exp(\epsilon_m^\wedge) = \mathbf{T}_m \exp\left(\begin{bmatrix} \rho_m \\ \phi_m \end{bmatrix}^\wedge\right). \quad (10)$$

Then the gradient with respect to ϵ_m is

$$\begin{aligned} \nabla F_{ij}^{mn} &= c_{ij}^{mn} \frac{\partial k(d(\mathbf{T}_m \exp(\epsilon_m^\wedge) \mathbf{x}_i^m, \mathbf{T}_n \mathbf{z}_j^n)^2)}{\partial d} \frac{\partial d}{\partial \epsilon_m} \\ &= c_{ij}^{mn} \frac{\partial k(d(\mathbf{T}_m \exp(\epsilon_m^\wedge) \mathbf{x}_i^m, \mathbf{T}_n \mathbf{z}_j^n)^2)}{\partial d} \frac{1}{d} \frac{\partial d}{\partial \epsilon_m} d \\ &= c_{ij}^{mn} k \frac{-2d}{2\ell^2} \frac{1}{d} \frac{\partial d}{\partial \epsilon_m} d \\ &= \frac{-1}{\ell^2} \underbrace{c_{ij}^{mn} k}_{w_{ij}^{mn}} \frac{\partial d}{\partial \epsilon_m} d, \end{aligned} \quad (11)$$

where we denote the term

$$w_{ij}^{mn} := c_{ij}^{mn} k(d(\mathbf{T}_m \exp(\epsilon_m^\wedge) \mathbf{x}_i^m, \mathbf{T}_n \mathbf{z}_j^n)^2) \quad (12)$$

After summing it up for all pairs of $(m, n) \in \mathcal{C}$ and $\mathbf{x}_i^m \in X_m$, $\mathbf{z}_j^n \in Z_n$ and taking the gradients to zero, we obtain

$$\sum_{(m,n) \in \mathcal{C}} \sum_{\substack{\mathbf{x}_i^m \in X_m \\ \mathbf{z}_j^n \in Z_n}} w_{ij}^{mn} \frac{\partial d}{\partial \epsilon_m} d = 0. \quad (13)$$

Here the weight w_{ij}^{mn} is a bounded number encoding the full geometric and semantic relations between the pair of points. In real data, a point's color or semantic features can differ from most other points. Thus, the weight will effectively suppress the originally dense residuals between this point and all the other points. If we treat w_{ij}^{mn} as *constant* weights during one optimization step, the solution to (13) corresponds to the solution for the following least squares problem:

$$\arg \max_{\mathcal{T}} \sum_{(m,n) \in \mathcal{C}} \sum_{\substack{\mathbf{x}_i^m \in X_m \\ \mathbf{z}_j^n \in Z_n}} w_{ij}^{mn} d(\mathbf{T}_m \mathbf{x}_i^m, \mathbf{T}_n \mathbf{z}_j^n)^2 \quad (14)$$

where \mathcal{T} are the poses of all the keyframes involved except the first frame. To see that, we can apply the perturbation $\exp(\epsilon_m^\wedge)$ on the right of \mathbf{T}_m and then take the gradient with respect to ϵ_m for (14). During the optimization, the weight value w_{ij}^{mn} is re-calculated after every step update due to the pose changes.

Problem (14) is a nonlinear least squares [37, 65, 76, 88] on the $SE(3)$ manifold that can be solved with an off-the-shelf solver like Ceres [3]. Please refer to the Appendix for the detailed derivation.

B. Convergence of the IRLS

Classical IRLS are widely used in solving robust non-linear problems. IRLS will converge to a stationary point [1] when a) The minimizer of the IRLS is a continuous function with respect to the weights. b) For the robust kernel $\rho(r)$, $\rho(\sqrt{r})$ is a concave and differentiable function. c) The weights are prevented from going to infinity when the residuals are becoming too large. Typical treatments include using truncated loss functions that suppress the effect of large residuals with solvers like Graduated Non-Convexity (GNC) [7, 85].

The convergence of the proposed IRLS is reached because a) The cost functions are continuous. b) the robust kernel in our objective function is $\rho(r) = -\exp(-\frac{r^2}{\ell^2})$ and $\rho(\sqrt{r}) = -\exp(-\frac{r}{\ell^2})$ is indeed concave and differentiable. c) This work's weight in Eq. (12) is a continuous and bounded function, whose values are less than or equal to 1.

C. Lengthscale Decay

In classical featured-based and photometric bundle adjustments, residuals are collected from image pyramids to consider feature points at different scales [25, 50]. In RKHS registration, point clouds are represented as continuous functions, where the lengthscale ℓ of the geometric kernel in (8) controls the scale [91]. In our implementation, we calculate the gradient of the full distance measure in (3) with respect to ℓ , to obtain the direction of ℓ 's change. Then ℓ is updated by a fixed percentage according to the direction.

VI. EXPERIMENTAL RESULTS

We evaluate the global rotation initialization and the multi-frame registration with publicly available datasets. We start with toy examples of two-frame global registration and four-frame multi-view registrations on partially overlapped geometric and semantic point clouds. The motivation is to stress-test the proposed method's performance under different initialization and outlier ratios. Next, to test its performance in actual applications, we present outdoor experiments with RGB-D and LiDAR datasets. The depth sources come from neural network predictions and LiDAR observations. We run the experiments on a desktop with a 48-core Intel(R) Xeon(R) Platinum 8160 CPU and an Nvidia Titan RTX GPU.

A. Simulated Example: Global Rotation Initialization

We use the Stanford Bunny point cloud scan [75] to test the global initialization under different rotation configurations. The two point clouds are initialized as follows. First, they are randomly rotated with two different angles, 90° and 180° , along a random axis. Second, random translations with length 0.5 are further applied. Third, we perturb the point clouds with point-wise Gaussian mixture noises. It has five different outlier ratios: 0%, 12.5%, 25%, 37.5%, and 50%. If it is sampled as an inlier, then we add a Gaussian perturbation $\mathcal{N}(0, 0.01)$ along the normal direction of the point. If it is an outlier, we also add a uniform noise between $(-0.1, 0.1)$ along the point's normal direction. Last but not least, we randomly crop

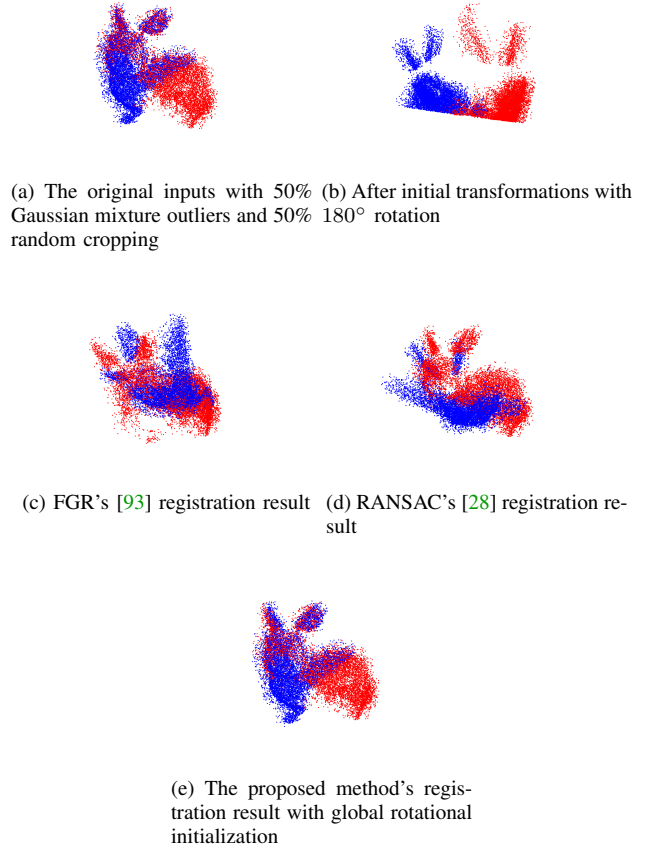


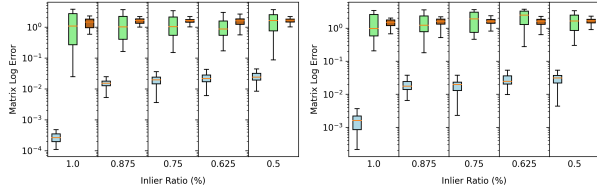
Fig. 2: An example of a two-view point cloud registration test with PPFH [59] invariant feature information on the Bunny [75] Dataset. (a) The two partially overlapped point clouds of the Bunny Dataset, each perturbed by 50% random outliers and 50% cropping. (b) The two Bunny point clouds after we apply initial rotations of 180 degrees around a random axis and a random translation of 0.5m. (c) FGR's registration result. (d) RANSAC's registration result. (e) The proposed method's registration results using global rotational initialization.

0%, 12.5%, 25%, 37.5%, and 50% of the two point clouds so that they do not fully overlap.

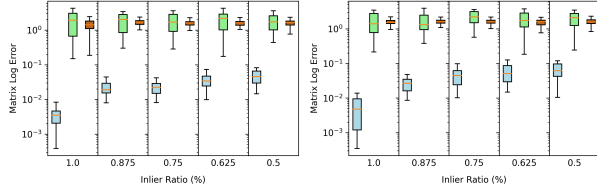
We first run the global rotation initialization scheme to select the best initial value, then run normal optimization of Eq. (4) to compute the relative pose. We compare our registration results with RANSAC [28] and FGR [93] which are two popular choices for global registration. For a fair comparison, all the methods use PPFH [59] features. The proposed method takes PPFH features in the label function $\ell_X(\mathbf{x})$ as in (2). We evaluate the relative pose predictions with the matrix logarithm error:

$$\log(\mathbf{T}_{\text{pred}}^{-1} \mathbf{G}^{(\text{gt})}) \quad (15)$$

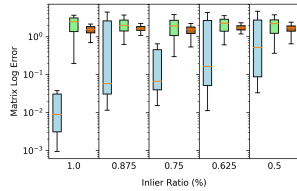
Fig. 2 shows the qualitative results of the proposed method versus the baselines, under 50% uniformly distributed outliers and 50% random cropping, when an unknown pose with 180° rotation is imposed. The initial data pair has fewer than 50% overlap. Under such perturbations, one-to-one data correspondence is challenging for classical methods. The



(a) Initial Rotation = 90° 0% cropping (b) Initial Rotation = 90° , 12.5% cropping



(c) Initial Rotation = 90° , 25% cropping (d) Initial Rotation = 90° , 37.5% cropping



(e) Initial Rotation = 90° , 50% cropping

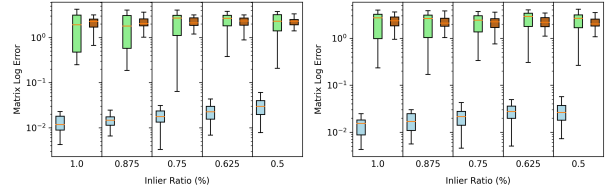
Fig. 3: The benchmark results of the two-frame registrations on the Bunny Dataset [75]. The three methods in the plots include: **Blue**: RKHS Registration with Global Rotation Initialization, **Green**: RANSAC [28], **Purple**: FGR [93]. Each box plot contains the resulting pose errors in the norm of matrix logarithm under different outlier ratios and cropping ratios at the same 90° initial rotation angle. (a) 0% cropping (b) 12.5% cropping (c) 25% cropping (d) 37.5% cropping (e) 50% cropping.

proposed method can retrieve the correct transformation while the baselines cannot.

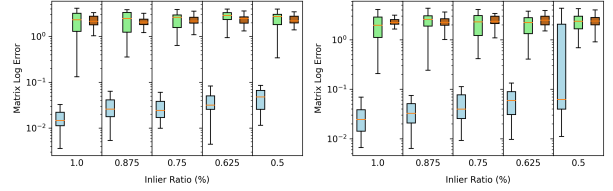
Fig. 3 and Fig. 4 show the quantitative results of the proposed global rotation initialization versus the baselines when unknown poses with 90° and 180° rotation are imposed, under a range of various outlier ratio and cropping ratio. The proposed method can retrieve the correct transformation compared to the baselines. Under such large angles, the baselines cannot correctly regress the correct transformation. In contrast, the proposed method has a relatively low error ($< 1e^{-2}$) when the cropping ratio is less than 37.5%. The errors increase significantly when the cropping ratio reaches 50% at both angles. The two figures show the proposed method’s superior robustness under large angles and the existence of outliers.

B. Simulated Example of Multi-point cloud registration

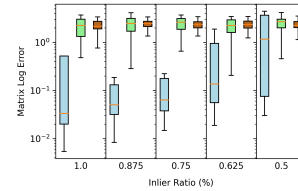
We present two toy examples of multi-frame registration on the Stanford Bunny dataset [75], shown in Figure 5, and the TartanAir dataset [79], shown in Figure 6. The Bunny Dataset provides only geometric point clouds. The TartanAir Dataset provides color and semantic point clouds. We choose four scans that do not completely overlap. They are further downsampled with a voxel filter.



(a) Initial Rotation = 180° , 0% cropping (b) Initial Rotation = 180° , 12.5% cropping



(c) Initial Rotation = 180° , 25% cropping (d) Initial Rotation = 180° , 37.5% cropping



(e) Initial Rotation = 180° , 50% cropping

Fig. 4: The benchmark results of the two-view registration on the Bunny Dataset [75]. The three methods in the plots include: **Blue**: RKHS Registration with Global Rotation Initialization, **Green**: RANSAC [28], **Purple**: FGR [93]. Each box plot contains the resulting pose errors in the norm of matrix logarithm under different outlier ratios and cropping ratios at the same 180° initial rotation angle. (a) 0% cropping (b) 12.5% cropping (c) 25% cropping (d) 37.5% cropping (e) 50% cropping.

The four point clouds are initialized as follows. First, they are randomly rotated with four different angles, 12.5° , 25° , 37.5° , and 50° , along a random axis. Second, random translations are further applied. Third, we perturb the point clouds with five different outlier ratios: 0%, 12.5%, 25%, 37.5%, and 50%. A perturbation is added in the normal direction of every point. If a point is an outlier, a uniformly sampled noise is added in the specified interval around the point. Otherwise, we add a Gaussian noise centered around the point’s original position. We generate 40 random initializations for each angle and outlier ratio pair above.

We compare our registration results with JRMPCC [27], which is a multi-frame geometric registration baseline based on Gaussian Mixture Model (GMM). We evaluate a single registration result with the sum of Frobenius Norm (denoted as $\|\cdot\|_F$) of the errors of the other three frames’ poses with respect to the first frame,

$$\sum_{i=2}^4 \|\mathbf{T}_i^{-1} \mathbf{G}_i^{(gt)} - \mathbf{I}\|_F.$$

where $\mathbf{G}_i^{(gt)} \in SE(3)$ is the ground truth pose.

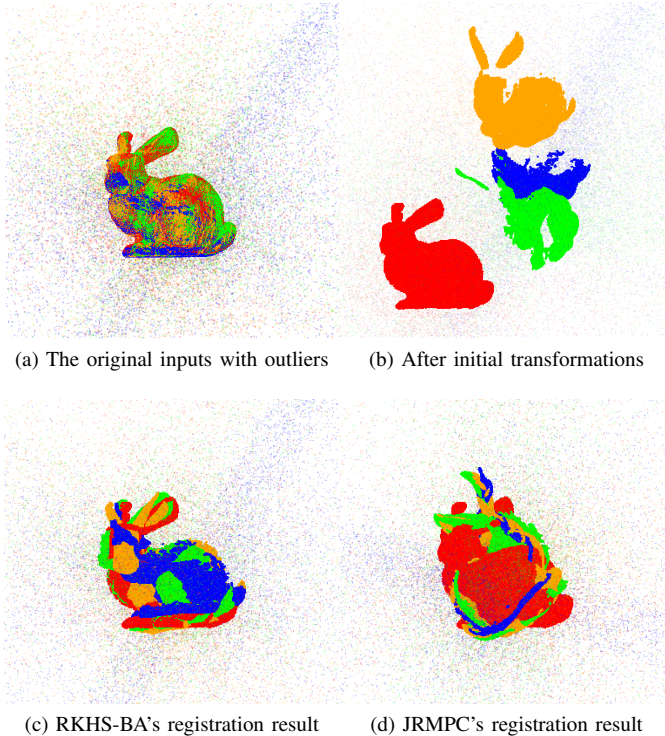


Fig. 5: An example of a four-view point cloud registration test with only geometric information on the Bunny [75] Dataset. (a) The four partially-overlapped point clouds of the Bunny Dataset, each perturbed by 50% random outliers. (b) The four Bunny point clouds after we apply initial rotations of 50 degrees around random axes and a random translation of $0.5m$. (c) RKHS-BA's registration result. (d) JRMPC's [27] registration result. $\gamma = 0.1$.

1) *Multi-Point Cloud geometric registration:* In the Bunny dataset [75], we choose four frames that are not fully overlapped from the original scan. The norms of the random initial translations are less than $1m$. The uniform noise for every outlier point is randomly sampled from the $[-0.5m, +0.5m]$ interval. The Gaussian noise for every inlier point is centered around the point's original position with a standard deviation of $0.01m$. In this experiment, we also select two different outlier ratio parameter setups for JRMPC, denoted as γ in its paper. γ is a positive scalar specifying the proportion of outliers used to calculate the prior distribution in JRMPC.

We report the results for every outlier ratio and initial angle pair with box plots in Fig. 9 and the error Cumulative Distribution Function (CDF) plot in Fig. 7a. JRMPC has slightly lower errors when the outlier ratio is small but is not robust when the outlier ratio grows above 25%. RKHS-BA is not sensitive to a larger outlier ratio. It can achieve consistently low errors in most of the experiment cases. In this experiment, a larger outlier ratio ($\gamma = 0.5$) of JRMPC has slightly better performance than $\gamma = 0.1$. The error CDF plot in Figure 7a also shows that the baseline has more failed cases than the proposed method. The result of the Bunny registration experiment is visualized in Figure 5. We are able to achieve smaller errors compared to JRMPC.

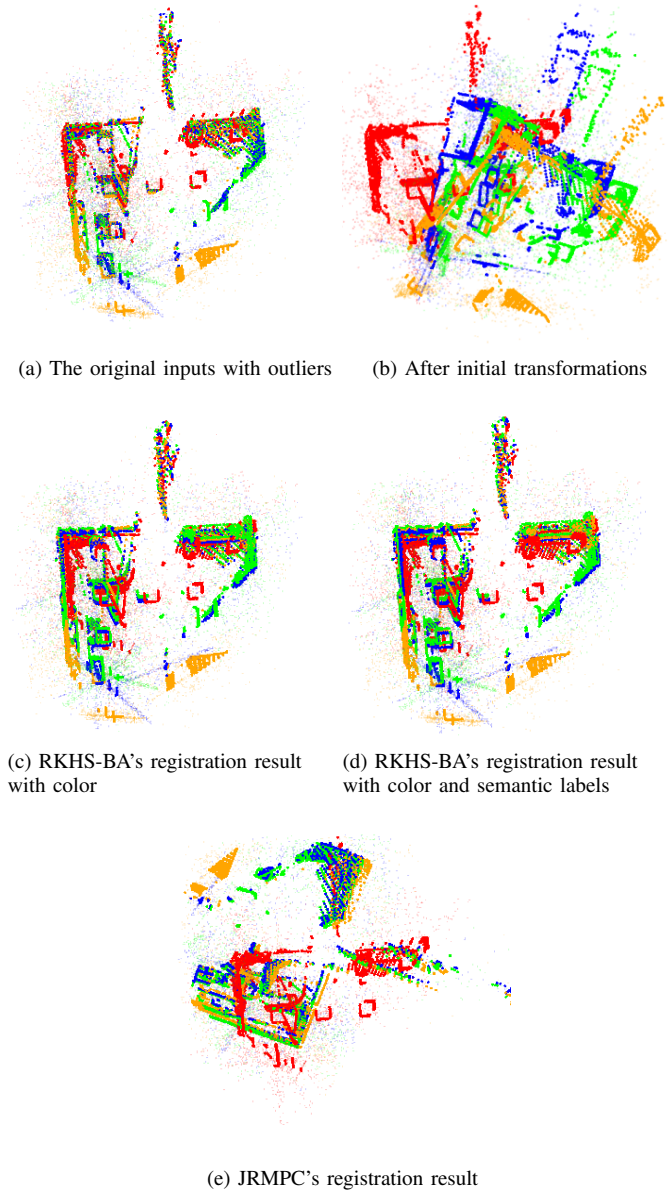
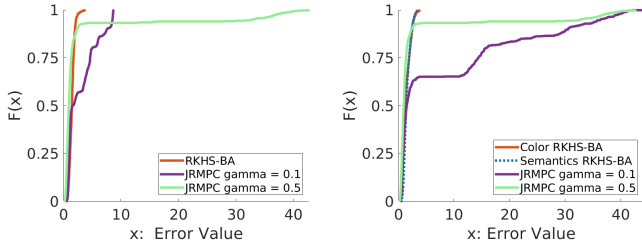
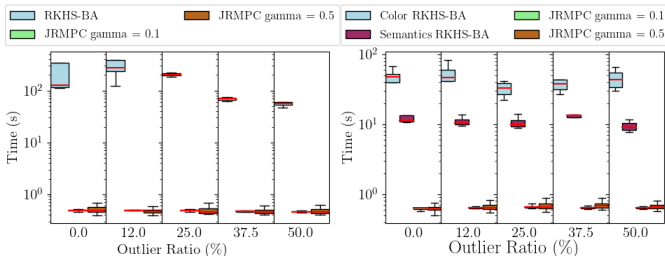


Fig. 6: An example of a four-view point cloud registration test on TartanAir-Wang et al. [79] Hospital-Easy-P001 sequence. The four point clouds are sampled every 20 frames. The semantic labels for every frame are provided by the dataset. (a) The initial four different frames of the TartanAir Dataset, each perturbed by 50% random outliers. (b) The four Tartanair point clouds after we apply initial rotations of 50 degrees around random axes and a random translation of $4m$. (c) RKHS-BA's registration result with only color information. (d) RKHS-BA's registration result with both color and semantic labels. (e) JRMPC's Evangelidis and Horaud [27] registration result with $\gamma = 0.1$.



(a) CDF for Bunny registration test (b) CDF for TartanAir registration test

Fig. 7: The error CDF plot of all the four-view point cloud registration tests on the Bunny [75] and TartanAir [79] Dataset (a) The error CDF for all the Bunny experiments. (b) The error CDF for all the TartanAir experiments.



(a) Time for Bunny registration test (b) Time for TartanAir registration test

Fig. 8: The running time statistics for a single four-view registration of all the experiments. (a) Box Plot for the registration time on the Bunny Dataset Turk [75] (b) Box Plot for the registration time on the TartanAir Dataset Wang et al. [79]

2) *Multi-Point Cloud color and semantic registration:* In the TartanAir dataset [79], we choose four frames from the Hospital-Easy-P001 indoor sequence. The four point clouds are sampled every 20 frames. The norms of the random initial translations are less than $4m$. The uniform noise for every outlier point is randomly sampled from the $[-4m, +4m]$ interval. The Gaussian noise for every inlier point is centered around the point’s original position with a standard deviation of $0.4m$. We also use the same outlier ratio parameter setups for JRMPC as in the Bunny Experiment.

As shown in Fig. 10, the Color and Semantic RKHS-BA have similar errors under different initial rotations and outlier rates. JRMPC is sensitive to the choice of the outlier ratio parameter γ . It has significantly larger errors at all the initial values when $\gamma = 0.1$. It has lower errors at larger actual outlier rates (37.5% and 50%), but is also not robust when the actual outlier rate is 25%. According to the CDF plot in Figure 7b, when $\gamma = 0.1$, JRMPC achieves better performance than the case when $\gamma = 0.5$, but it still has more failed case than our method. The result of the TartanAir registration experiment is visualized in Figure 6. We can achieve small errors even when the outlier ratio is very large.

3) *Time Analysis:* Assuming there are M edges in the pose graph and each frame has $O(N)$ points, then the time complexity would be $O(MN^2)$ because of the cost to evaluate all pairs of inner product values.

The time consumption in the four-frame registration tests

is listed in Fig. 8. JRMPC is significantly faster in all the examples. Interestingly, the additional hierarchical semantic information improves RKHS-BA’s running speed because it helps sparsify the number of nontrivial inner products.

C. Application: Sliding Window Semantic Bundle Adjustment

We evaluate the proposed BA algorithm on multiple sequences of the TartanAir Dataset [79]. We present quantitative evaluations of the trajectories as well as qualitative comparisons of the stacked point cloud maps versus the mainstream algorithms. We present semantic BA results on the TartanAir dataset [79]. The TartanAir dataset contains photo-realistic simulations of environments with ground truth depth and semantic measurements. We select sequences that include different weather conditions to demonstrate the robustness of the proposed method. The input depth images are generated with Unimatch [84] from stereo image pairs. The semantic segmentation labels provided in the dataset are raw object IDs generated by the simulator. We merge less frequent IDs into a single class, resulting in a total of 10 classes at max. In the quantitative comparison, we calculate the drift in Absolute Translation Error (ATE) in meters using the evaluation tool provided by TartanAir [79].

1) *Baseline setup:* In the experiments, we implement the proposed formulation into a frontend and a backend. The frontend is the frame-to-frame tracking as in SemanticCVO [91] and provides initial pose values for the backend. It takes around 2000 semi-dense points from an input image generated with DSO [24]’s point selector. The backend uses the full inner product formulation (7) on the latest four keyframes and estimates the final poses. Both datasets use fixed sets of hyperparameters within their sequences.

We compare our approach with four visual SLAM or odometry systems: BAD-SLAM [62], ORB-SLAM2 [50], ElasticFusion [81] and StereoDSO [78]. StereoDSO is the closest baseline because of its backend’s semi-dense photometric bundle adjustment. BAD-SLAM and ElasticFusion both feature a joint color and geometric optimization in the backend, although they have independent map fusion steps. With a featured-based bundle adjustment module, ORB-SLAM2 does not share the same perspective as direct SLAMs but is listed here for reference. We use BAD-SLAM, ORB-SLAM2, and ElasticFusion’s officially released code with RGB-D inputs. Since StereoDSO’s original implementation is not released, we reproduced DSO’s results using an open-source implementation [83], which contains DSO with stereo depth initialization. For a fair comparison, all the methods’ global loop closure modules are turned off.

The quantitative results are listed in Table I. The qualitative comparisons of all the methods on three challenging sequences are shown in Figure 11. The point cloud mapping results of our method and baselines in the hospital sequence are shown in Figure 12. RKHS-BA which takes color point clouds has lower mean drifts ($0.664m$) than the remaining direct methods with color or intensity inputs. RKHS-BA with both color and semantic inputs outperforms Color RKHS-

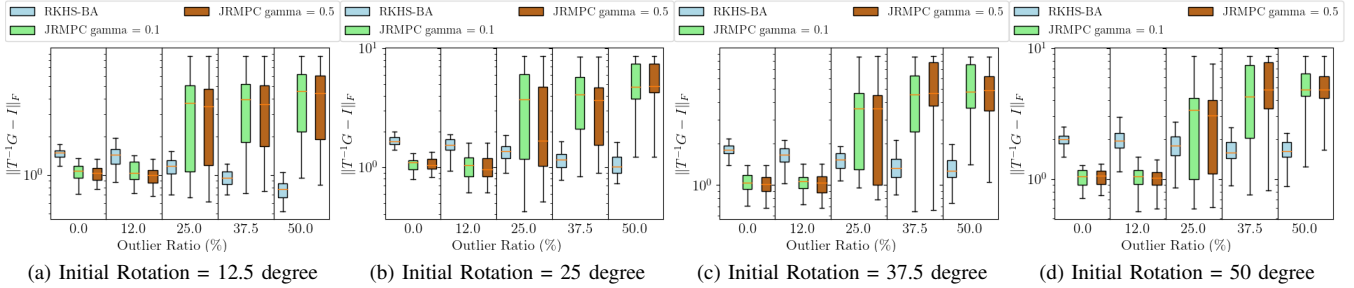


Fig. 9: The benchmark results of the four-frame registration tests on the Bunny Dataset [75]. Each box plot contains the resulting pose errors in the Frobenius Norm of different outlier ratios at the same initial rotation angle. (a) The initial angle is 12.5 degrees. (b) The initial angle is 25 degrees. (c) The initial angle is 37.5 degrees. (d) The initial angle is 50 degrees.

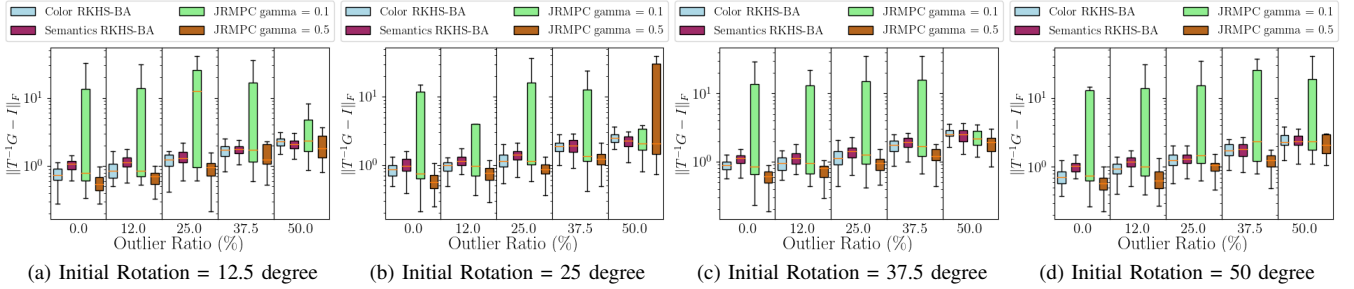


Fig. 10: The benchmark results of the four-frame registration test on the TartanAir Dataset [79]. We include both Color RKHS-BA which takes color information, as well as Semantic RKHS-BA which takes both color and semantic labels. Each box plot contains the resulting pose errors in the Frobenius Norm of different outlier ratios at the same initial rotation angle. (a) The initial angle is 12.5 degrees. (b) The initial angle is 25 degrees. (c) The initial angle is 37.5 degrees. (d) The initial angle is 50 degrees.

BA (0.584m). Both demonstrate a small standard deviation in the results as well. Feature based method still performs the best on the two well-structured sequences, *gascola* and *seasonsforest*, when it is able to complete. But in sequences with repetitive patterns, such as *hospital*, data association becomes difficult for feature-based backends. Furthermore, in sequences with dynamic weather, like the rainy *soulcity*, the images are contaminated with raindrops and water reflections. As shown in Figure 11c, even direct backends cannot do well, while the color and semantic RKHS-BA still report low translation errors.

D. Application: LiDAR Global Mapping

LiDAR global mapping is another application of RKHS-BA. Classical LiDAR SLAM methods perform pose graph optimization (PGO) after loops are detected, but PGO only considers the consistency of poses without the consistency of the map [44]. In contrast, camera-based visual SLAMs [50] add an extra step besides PGO, that is, global bundle adjustment, to enforce the consistency of the map across frames as well.

1) *Setup*: Assuming the trajectory of PGO is given, we construct a pose graph for RKHS-BA. For any frame f_i , we firstly connect its adjacent frames f_{i-1} and f_{i+1} , then the frames whose translation is within a 1-meter boundary of the frame f_i . All the edges are assigned an initial lengthscale 0.075.

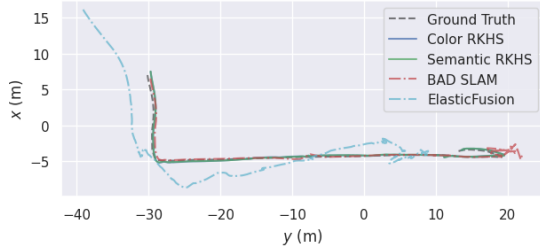
In addition, due to the large number of LiDAR points per frame, we downsample the input point clouds with voxel filters. To make sure that each frame has enough line points and surface points, we use 0.4m voxels for surfaces and 0.1m for lines. This ensures that each frame contains less than 10,000 points.

We benchmark the proposed method and the baselines on the SemanticKITTI LiDAR dataset [5]. Using the same set of hyperparameters, we evaluate the proposed method on seven sequences, 00, 02, 05, 06, 07, 08, 09 that have loop closures. We use the official evaluation tool from KITTI’s website, which measures the translational drift, as a percentage (%), and the rotational drift, in degrees per meter($^{\circ}/m$) on all possible subsequences of 100, 200..., 800 meters.

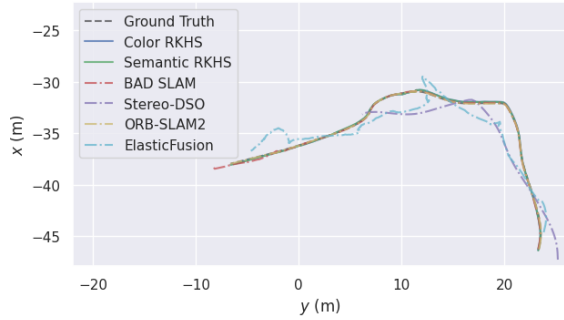
2) *Baselines*: The baselines of the proposed BA formulation are the point-to-line and point-to-plane distances in the mainstream LiDAR bundle adjustment methods. The initial odometry comes from MULLS’s [55] PGO result. We choose BALM [44] and HBA [43] as baselines because they provide open-source implementations. Note that BALM and HBA have extra components, such as hierarchical submaps, other than optimizing the point-to-feature costs themselves. We enable these additional modules for the completeness of their camera implementations. The baselines also use the same initial poses from PGO and the same input point clouds as RKHS-BA.

TABLE I: Results of the proposed frame-to-frame method using the TartanAir benchmark as evaluated on the ATE in meters. If a method doesn't complete a sequence, the frame's index with lost tracking will be recorded in the parenthesis.

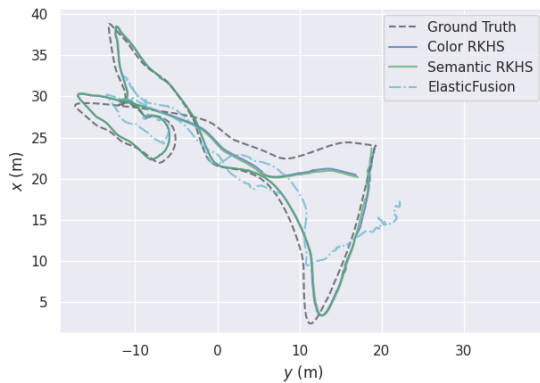
Sequence (Easy P001)	Environment	No. Frames	Semantic-based direct method		Intensity-based direct method				Feature-based method
			Semantic RKHS ATE (m)	Semantic CVO [91] ATE (m)	Color RKHS ATE (m)	DSO-Stereo [83] ATE (m)	BAD SLAM [62] ATE (m)	ElasticFusion [81] ATE (m)	ORB-SLAM2 [50]
abandonedfactory	Sunny	434	0.3010	4.3293	0.3149	(412)	1.3642	8.0056	(410)
gascola	Foggy	382	0.0878	0.1388	0.0905	5.4988	0.1893	1.7340	0.0377
hospital	Repetitive	480	0.5535	1.3106	0.5675	0.9567	(434)	2.8675	(238)
seasonsforest	Forest	319	0.1399	0.1720	0.1395	(307)	17.0627	1.7279	0.0359
seasonsforest winter	Snowy	847	1.1515	1.8232	1.5631	7.4030	(591)	14.4673	(582)
soulcity	Rainy	1083	1.4628	5.1105	1.4563	(910)	(271)	5.6583	(480)
seasidetown	Textureless	403	0.3901	0.4311	0.3761	(30)	218.9929	4.9269	(260)
Mean	-	-	0.5838	1.9022	0.6440	-	-	5.6263	-
STD	-	-	0.5254	2.0334	0.6126	-	-	4.5148	-



(a) abandonedfactory sequence.



(b) gascola sequence.



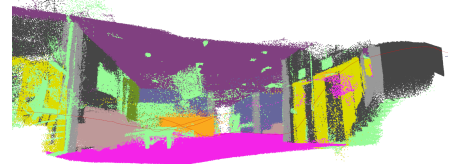
(c) soulcity sequence.

Fig. 11: Trajectories of the proposed method (solid line), baselines (dash-dot line), and ground truth (dashed line) on three TartanAir Wang et al. [79] sequences. Only baselines that successfully complete the sequences are plotted.

3) *Experiment Results:* Table II shows the quantitative comparisons between the proposed intensity-based and semantic-based global bundle adjustments. The proposed intensity-based BA has improvements on the initial values



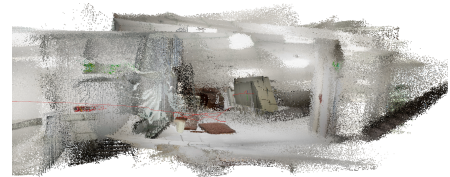
(a) Color RKHS-BA.



(b) Semantics RKHS-BA.



(c) DSO.



(d) Elastic Fusion.

Fig. 12: Qualitative comparisons of the stacked point cloud map of the four methods above in the TartanAir hospital sequence. We use the poses from their result trajectories and the raw point cloud inputs. RKHS-BA in (a) and (b) reconstruct the stairs and the wall on the right side consistently. DSOEngel et al. [24] in (c) fails to reconstruct the wall on the right, and the floor is cracked. ElasticFusionWhelan et al. [81] in (d) can hardly show the structure of the hospital rooms. ORB-SLAM2Mur-Artal and Tardós [50]'s result is not plotted because it doesn't complete the sequence.

from the MULLS' pose graph optimization on all the sequences. This indicates that BA methods that consider the map consistency is indeed able to further refine the trajectory from the pose graph. Furthermore, RKHS-BA has better average errors and standard deviations than the baselines adopting point-to-feature loss as well, illustrating the effect of not relying on strict correspondence. Last but not least, the semantic RKHS-BA outperforms intensity-based alternative.

TABLE II: We compare the proposed RKHS-BA of color and semantic features with other state-of-the-art LiDAR local and global bundle adjustment methods [43, 44, 55] on seven SemanticKITTI [5] LiDAR sequences that contain loop closures: Sequence 00, 02, 05, 06, 07, 09. All the methods start from the same initial trajectories from MULLS [55] and the same downsampled point clouds. The assessments of errors are based on the drifts in translation, presented as a percentage (%), and rotation, measured in degrees per meter (°/m). The errors are computed for all subsequences of 100, 200, ..., 800 meters. The proposed methods have the lowest mean and standard deviation on translation and rotational errors.

Sequence	Semantic RKHS-BA		Intensity RKHS-BA		MULLS [55]		BALM [44]		HBA [43]	
	Trans. Errors	Rot. Errors	Trans. Errors	Rot. Errors	Trans. Errors	Rot. Errors	Trans. Errors	Rot. Errors	Trans. Errors	Rot. Errors
Seq 00	0.4602	0.0018	0.4620	0.0018	0.5841	0.0019	0.7669	0.0036	0.4097	0.0024
Seq 02	0.5989	0.0018	0.5990	0.0018	0.6936	0.0017	-	-	1.0782	0.0047
Seq 05	0.4897	0.0027	0.4914	0.0027	0.5837	0.0028	0.5158	0.0029	0.6097	0.0034
Seq 06	0.5057	0.0036	0.5068	0.0036	0.5211	0.0039	0.6598	0.0051	0.4256	0.0030
Seq 07	0.5487	0.0033	0.5500	0.0033	0.6678	0.0039	0.4582	0.0045	0.5429	0.0046
Seq 08	1.0836	0.0042	1.0866	0.0042	1.1867	0.0044	1.1391	0.0048	1.6308	0.0069
Seq 09	0.6254	0.0017	0.6303	0.0017	0.8215	0.0019	0.7703	0.0026	0.6023	0.0035
Mean	0.6160	0.0027	0.6180	0.0027	0.7226	0.0030	0.7183	0.0039	0.7570	0.0041
STD	0.2144	0.0010	0.2151	0.0010	0.2266	0.0011	0.2426	0.0010	0.4451	0.0015

VII. DISCUSSIONS AND LIMITATIONS

A. Baselines of the TartanAir Experiments

Besides the baseline results reported above, we also test DSO’s photometric backend with the same frontend tracking as RKHS-BA on the TartanAir Dataset, but the improvement on the final ATE error on the *gascola* sequence is marginal, from $5.4988m$ to $5.4895m$, while still not able to complete other sequences. This indicates that its photometric bundle adjustment is not as robust as the proposed method in highly semi-static environments.

B. Lengthscale Choice

In the experiments, we notice that the initial lengthscale choice affects the gradient calculation. The traditional energy functions have larger values when the point clouds are far away. However, if the initial lengthscale is not large enough in RKHS-BA, the proposed formulation will have smaller inner product values in the same situation, which will lead to vanishing gradients. To address this problem, the optimization starts with a sufficiently large lengthscale at the cost of more computation time.

C. How do semantics help the registration practically?

From the results in Sec. VI, the added semantic information invariant to pose changes aid the function space RKHS registration in the following ways: a) Better soft association at larger initial angles: We have tested the 180° registration and without the FPFH features, and the registrations do not converge to the right rotation. a) Faster convergence time: In Fig. 8, the extra pixel labels reduce the running time by an order of magnitude. This is because when a point pair’s semantic kernel is small enough, we omit the geometry kernel computation for it as well. c) Slightly lower drift: As in Table I and Table II, both semantic BA results have slightly lower errors than the intensity-based versions.

VIII. CONCLUSION

We present RKHS-BA, a novel batch bundle adjustment formulation without explicit data association. It provides a systematic and natural way for multiple input frames to encode various semantic information and geometric information into a

joint function representation in the Reproducing Kernel Hilbert Space. Related applications include the backend pose graph optimizations of semi-dense visual SLAM systems. RKHS-BA obtains comparable accuracy in structured environments with mainstream semi-dense photometric bundle adjustment methods and outperforms them in more challenging semi-static environments, even with significant outliers.

Future work will focus on implementing the inner product calculations with GPU processors because of its natural parallel structure. In addition, a dense semantic mapping technique can be integrated with the current bundle adjustment framework as a complete direct semantic SLAM system.

REFERENCES

- [1] Khuram Aftab and Richard Hartley. Convergence of iteratively re-weighted least squares to robust estimators. In *2015 IEEE Winter Conference on Applications of Computer Vision*, pages 480–487, 2015. doi: 10.1109/WACV.2015.70. 6
- [2] Pratik Agarwal, Gian Diego Tipaldi, Luciano Spinello, Cyrill Stachniss, and Wolfram Burgard. Robust map optimization using dynamic covariance scaling. In *Proc. IEEE Int. Conf. Robot. and Automation*, pages 62–69. Ieee, 2013. 3
- [3] Sameer Agarwal and Keir Mierle. Ceres solver: Tutorial & reference. *Google Inc*, 2(72):8, 2012. 5
- [4] Pasquale Antonante, Vasileios Tzoumas, Heng Yang, and Luca Carlone. Outlier-robust estimation: Hardness, minimally tuned algorithms, and applications. *IEEE Transactions on Robotics*, 38(1):281–301, 2021. 2
- [5] Jens Behley, Martin Garbade, Andres Milioto, Jan Quenzel, Sven Behnke, Cyrill Stachniss, and Jurgen Gall. SemanticKITTI: A dataset for semantic scene understanding of lidar sequences. In *Proceedings of the IEEE/CVF international conference on computer vision*, pages 9297–9307, 2019. 2, 10, 12
- [6] Christopher M. Bishop. *Pattern Recognition and Machine Learning*. Springer-Verlag, Berlin, Heidelberg, 2006. ISBN 0387310738. 2
- [7] Michael J Black and Anand Rangarajan. On the unification of line processes, outlier rejection, and robust

- statistics with applications in early vision. *International journal of computer vision*, 19(1):57–91, 1996. 6
- [8] Michael Bloesch, Jan Czarnowski, Ronald Clark, Stefan Leutenegger, and Andrew J Davison. Codeslam—learning a compact, optimisable representation for dense visual slam. In *Proceedings of the IEEE conference on computer vision and pattern recognition*, pages 2560–2568, 2018. 3
- [9] Sean L Bowman, Nikolay Atanasov, Kostas Daniilidis, and George J Pappas. Probabilistic data association for semantic slam. In *Proc. IEEE Int. Conf. Robot. and Automation*, pages 1722–1729. IEEE, 2017. 3
- [10] Cesar Cadena, Luca Carlone, Henry Carrillo, Yasir Latif, Davide Scaramuzza, José Neira, Ian Reid, and John J. Leonard. Past, present, and future of simultaneous localization and mapping: Toward the robust-perception age. *IEEE Trans. Robot.*, 32(6):1309–1332, 2016. doi: 10.1109/TRO.2016.2624754. 2
- [11] X. Chen, A. Milioto, E. Palazzolo, P. Giguère, J. Behley, and C. Stachniss. Suma++: Efficient lidar-based semantic slam. In *Proc. IEEE/RSJ Int. Conf. Intell. Robots and Syst.*, pages 4530–4537, 2019. doi: 10.1109/IROS40897.2019.8967704. 1
- [12] William Clark, Maani Ghaffari, and Anthony Bloch. Nonparametric continuous sensor registration. *J. Mach. Learning Res.*, 22(271):1–50, 2021. 2, 4, 5
- [13] Taco Cohen, Maurice Weiler, Berkay Kicanaoglu, and Max Welling. Gauge equivariant convolutional networks and the icosahedral cnn. In *International conference on Machine learning*, pages 1321–1330. PMLR, 2019. 5
- [14] Jan Czarnowski, Tristan Laidlow, Ronald Clark, and Andrew J Davison. Deepfactors: Real-time probabilistic dense monocular slam. *IEEE Robotics and Automation Letters*, 5(2):721–728, 2020. 3
- [15] Angela Dai, Matthias Nießner, Michael Zollhöfer, Shahram Izadi, and Christian Theobalt. Bundlefusion: Real-time globally consistent 3d reconstruction using on-the-fly surface reintegration. *ACM Transactions on Graphics (ToG)*, 36(4):1, 2017. 2
- [16] Martin Danelljan, Giulia Meneghetti, Fahad Shahbaz Khan, and Michael Felsberg. A probabilistic framework for color-based point set registration. In *Proc. IEEE Conf. Comput. Vis. Pattern Recog.*, pages 1818–1826, 2016. 2
- [17] A. J. Davison, I. D. Reid, N. D. Molton, and O. Stasse. Monoslam: Real-time single camera slam. *IEEE Trans. Pattern Anal. Mach. Intell.*, 29(6):1052–1067, 2007. doi: 10.1109/TPAMI.2007.1049. 1
- [18] Andrew J Davison. Real-time simultaneous localisation and mapping with a single camera. In *Proc. IEEE Int. Conf. Comput. Vis.*, volume 3, pages 1403–1403. IEEE Computer Society, 2003. 1
- [19] Pierre Dellenbach, Jean-Emmanuel Deschaud, Bastien Jacquet, and François Goulette. Ct-icp: Real-time elastic lidar odometry with loop closure. In *2022 International Conference on Robotics and Automation (ICRA)*, pages 5580–5586. IEEE, 2022. 3
- [20] Kevin Doherty, Dehann Fourie, and John Leonard. Multimodal semantic slam with probabilistic data association. In *Proc. IEEE Int. Conf. Robot. and Automation*, pages 2419–2425. IEEE, 2019. 1, 3
- [21] Kevin J Doherty, David P Baxter, Edward Schneeweiss, and John J Leonard. Probabilistic data association via mixture models for robust semantic slam. In *Proc. IEEE Int. Conf. Robot. and Automation*, pages 1098–1104. IEEE, 2020. 3
- [22] Kevin J Doherty, Ziqi Lu, Kurran Singh, and John J Leonard. Discrete-Continuous Smoothing and Mapping. *arXiv preprint arXiv:2204.11936*, 2022. 1
- [23] Kevin J. Doherty, Ziqi Lu, Kurran Singh, and John J. Leonard. Discrete-Continuous Smoothing and Mapping. *IEEE Robotics and Automation Letters*, 7(4):12395–12402, 2022. doi: 10.1109/LRA.2022.3216938. 1
- [24] J. Engel, V. Koltun, and D. Cremers. Direct sparse odometry. *IEEE Trans. Pattern Anal. Mach. Intell.*, 40(3):611–625, March 2018. ISSN 0162-8828. doi: 10.1109/TPAMI.2017.2658577. 1, 2, 9, 11
- [25] Jakob Engel, Thomas Schöps, and Daniel Cremers. Lsdslam: Large-scale direct monocular slam. In *Proc. European Conf. Comput. Vis.*, pages 834–849. Springer, 2014. 2, 3, 6
- [26] Jakob Engel, Vladlen Koltun, and Daniel Cremers. Direct sparse odometry. *IEEE Trans. Pattern Anal. Mach. Intell.*, 40(3):611–625, 2017. 1, 2, 3
- [27] Georgios Dimitrios Evangelidis and Radu Horaud. Joint alignment of multiple point sets with batch and incremental expectation-maximization. *IEEE Trans. Pattern Anal. Mach. Intell.*, 40(6):1397–1410, 2017. 7, 8
- [28] Martin A Fischler and Robert C Bolles. Random sample consensus: a paradigm for model fitting with applications to image analysis and automated cartography. *Communications of the ACM*, 24(6):381–395, 1981. 6, 7
- [29] C. Forster, M. Pizzoli, and D. Scaramuzza. Svo: Fast semi-direct monocular visual odometry. In *Proc. IEEE Int. Conf. Robot. and Automation*, pages 15–22, 2014. doi: 10.1109/ICRA.2014.6906584. 2
- [30] Dehann Fourie, John Leonard, and Michael Kaess. A nonparametric belief solution to the bayes tree. In *Proc. IEEE/RSJ Int. Conf. Intell. Robots and Syst.*, pages 2189–2196, 2016. doi: 10.1109/IROS.2016.7759343. 3
- [31] Maani Ghaffari, William Clark, Anthony Bloch, Ryan M. Eustice, and Jessie W. Grizzle. Continuous direct sparse visual odometry from RGB-D images. In *Proc. Robot.: Sci. Syst. Conf.*, Freiburg, Germany, June 2019. 3, 5
- [32] Ross Girshick. Fast r-cnn. In *Proceedings of the IEEE international conference on computer vision*, pages 1440–1448, 2015. 1
- [33] Zan Gojcic, Caifa Zhou, Jan D Wegner, and Andreas Wieser. The perfect match: 3d point cloud matching with smoothed densities. In *Proc. IEEE Conf. Comput. Vis. Pattern Recog.*, pages 5545–5554, 2019. 1
- [34] Jacob Goldberger. Registration of multiple point sets using the em algorithm. In *Proceedings of the Seventh IEEE*

- International Conference on Computer Vision*, volume 2, pages 730–736. IEEE, 1999. 2
- [35] Giorgio Grisetti, Rainer Kümmerle, Hauke Strasdat, and Kurt Konolige. g2o: A general framework for (hyper) graph optimization. In *Proc. IEEE Int. Conf. Robot. and Automation*, pages 9–13, 2011. 2
- [36] R. I. Hartley and A. Zisserman. *Multiple View Geometry in Computer Vision*. Cambridge University Press, ISBN: 0521540518, second edition, 2004. 1, 3
- [37] Gibson Hu, Kasra Khosoussi, and Shoudong Huang. Towards a reliable slam back-end. In *Proc. IEEE/RSJ Int. Conf. Intell. Robots and Syst.*, pages 37–43. IEEE, 2013. 5
- [38] Shahram Izadi, David Kim, Otmar Hilliges, David Molyneaux, Richard Newcombe, Pushmeet Kohli, Jamie Shotton, Steve Hodges, Dustin Freeman, Andrew Davison, et al. Kinectfusion: real-time 3d reconstruction and interaction using a moving depth camera. In *Proceedings of the 24th annual ACM symposium on User interface software and technology*, pages 559–568, 2011. 2
- [39] Michael Kaess, Hordur Johannsson, Richard Roberts, Viorela Ila, John J Leonard, and Frank Dellaert. isam2: Incremental smoothing and mapping using the bayes tree. *Int. J. Robot. Res.*, 31(2):216–235, 2012. 2
- [40] Christian Kerl, Jürgen Sturm, and Daniel Cremers. Dense visual slam for rgb-d cameras. In *Proc. IEEE/RSJ Int. Conf. Intell. Robots and Syst.*, pages 2100–2106. IEEE, 2013. 1, 2
- [41] Lukas Koestler, Nan Yang, Niclas Zeller, and Daniel Cremers. Tandem: Tracking and dense mapping in real-time using deep multi-view stereo. In *Conference on Robot Learning*, pages 34–45. PMLR, 2022. 3
- [42] Kenji Koide, Masashi Yokozuka, Shuji Oishi, and Atsuhiko Banno. Globally consistent 3d lidar mapping with gpu-accelerated gicp matching cost factors. *IEEE Robotics and Automation Letters*, 6(4):8591–8598, 2021. 3
- [43] Xiyuan Liu, Zheng Liu, Fanze Kong, and Fu Zhang. Large-scale lidar consistent mapping using hierarchical lidar bundle adjustment. *IEEE Robotics and Automation Letters*, 8(3):1523–1530, 2023. doi: 10.1109/LRA.2023.3238902. 3, 10, 12
- [44] Zheng Liu and Fu Zhang. Balm: Bundle adjustment for lidar mapping. *IEEE Robotics and Automation Letters*, 6(2):3184–3191, 2021. 3, 10, 12
- [45] David G Lowe. Distinctive image features from scale-invariant keypoints. *International journal of computer vision*, 60:91–110, 2004. 3
- [46] Zhe Min, Jiaole Wang, and Max Q-H Meng. Joint rigid registration of multiple generalized point sets with hybrid mixture models. *IEEE Transactions on Automation Science and Engineering*, 17(1):334–347, 2019. 2
- [47] Zhixiang Min, Yiding Yang, and Enrique Dunn. Voldor: Visual odometry from log-logistic dense optical flow residuals. In *Proc. IEEE Conf. Comput. Vis. Pattern Recog.*, pages 4898–4909, 2020. 2
- [48] Niloy J Mitra, Natasha Gelfand, Helmut Pottmann, and Leonidas Guibas. Registration of point cloud data from a geometric optimization perspective. In *Proceedings of the 2004 Eurographics/ACM SIGGRAPH symposium on Geometry processing*, pages 22–31, 2004. 3
- [49] Beipeng Mu, Shih-Yuan Liu, Liam Paull, John Leonard, and Jonathan P How. Slam with objects using a nonparametric pose graph. In *Proc. IEEE/RSJ Int. Conf. Intell. Robots and Syst.*, pages 4602–4609. IEEE, 2016. 3
- [50] Raul Mur-Artal and Juan D Tardós. Orb-slam2: An open-source slam system for monocular, stereo, and rgb-d cameras. *IEEE Trans. Robot.*, 33(5):1255–1262, 2017. 1, 6, 9, 10, 11
- [51] Raul Mur-Artal, Jose Maria Martinez Montiel, and Juan D Tardos. Orb-slam: a versatile and accurate monocular slam system. *IEEE Trans. Robot.*, 31(5):1147–1163, 2015. 2, 4
- [52] Richard A Newcombe, Steven J Lovegrove, and Andrew J Davison. Dtam: Dense tracking and mapping in real-time. In *2011 international conference on computer vision*, pages 2320–2327. IEEE, 2011. 1, 2
- [53] Edwin Olson and Pratik Agarwal. Inference on networks of mixtures for robust robot mapping. *Int. J. Robot. Res.*, 32(7):826–840, 2013. 1, 3
- [54] Joseph Ortiz, Talfan Evans, Edgar Sucar, and Andrew J. Davison. Incremental abstraction in distributed probabilistic slam graphs. In *Proc. IEEE Int. Conf. Robot. and Automation*, 2022. 1
- [55] Yue Pan, Pengchuan Xiao, Yujie He, Zhenlei Shao, and Zesong Li. Mulls: Versatile lidar slam via multi-metric linear least square. In *2021 IEEE International Conference on Robotics and Automation (ICRA)*, pages 11633–11640. IEEE, 2021. 3, 10, 12
- [56] David M Rosen, Kevin J Doherty, Antonio Terán Espinoza, and John J Leonard. Advances in inference and representation for simultaneous localization and mapping. *Annual Review of Control, Robotics, and Autonomous Systems*, 4:215–242, 2021. 1
- [57] Antoni Rosinol, John J Leonard, and Luca Carlone. Nerf-slam: Real-time dense monocular slam with neural radiance fields. *arXiv preprint arXiv:2210.13641*, 2022. 3
- [58] Ethan Rublee, Vincent Rabaud, Kurt Konolige, and Gary Bradski. Orb: An efficient alternative to sift or surf. In *Proc. IEEE Int. Conf. Comput. Vis.*, pages 2564–2571. Ieee, 2011. 3
- [59] Radu Bogdan Rusu, Nico Blodow, and Michael Beetz. Fast point feature histograms (fpfh) for 3d registration. In *2009 IEEE international conference on robotics and automation*, pages 3212–3217. IEEE, 2009. 6
- [60] Renato F. Salas-Moreno, Richard A. Newcombe, Hauke Strasdat, Paul H.J. Kelly, and Andrew J. Davison. Slam++: Simultaneous localisation and mapping at the level of objects. In *Proc. IEEE Conf. Comput. Vis. Pattern Recog.*, pages 1352–1359, 2013. doi: 10.1109/CVPR.2013.178. 1

- [61] Davide Scaramuzza and Friedrich Fraundorfer. Visual odometry [tutorial]. *IEEE robotics & automation magazine*, 18(4):80–92, 2011. 3
- [62] Thomas Schops, Torsten Sattler, and Marc Pollefeys. Bad slam: Bundle adjusted direct rgb-d slam. In *Proc. IEEE Conf. Comput. Vis. Pattern Recog.*, pages 134–144, 2019. 1, 2, 9, 11
- [63] Aleksandr Segal, Dirk Haehnel, and Sebastian Thrun. Generalized-ICP. In *Proc. Robot.: Sci. Syst. Conf.*, volume 2 Issue 4, page 435. Seattle, WA, 2009. 3
- [64] Tixiao Shan and Brendan Englot. Lego-loam: Lightweight and ground-optimized lidar odometry and mapping on variable terrain. In *Proc. IEEE/RSJ Int. Conf. Intell. Robots and Syst.*, pages 4758–4765. IEEE, 2018. 3
- [65] Hauke Strasdat, J Montiel, and Andrew J Davison. Scale drift-aware large scale monocular slam. *Robotics: Science and Systems VI*, 2(3):7, 2010. 3, 5
- [66] Edgar Sucar, Shikun Liu, Joseph Ortiz, and Andrew J Davison. imap: Implicit mapping and positioning in real-time. In *Proceedings of the IEEE/CVF International Conference on Computer Vision*, pages 6229–6238, 2021. 3
- [67] Niko Sünderhauf and Peter Protzel. Switchable constraints for robust pose graph slam. In *Proc. IEEE/RSJ Int. Conf. Intell. Robots and Syst.*, pages 1879–1884. IEEE, 2012. 3
- [68] Chengzhou Tang and Ping Tan. Ba-net: Dense bundle adjustment network. *arXiv preprint arXiv:1806.04807*, 2018. 3
- [69] Keisuke Tateno, Federico Tombari, Iro Laina, and Nassir Navab. Cnn-slam: Real-time dense monocular slam with learned depth prediction. In *Proc. IEEE Conf. Comput. Vis. Pattern Recog.*, pages 6243–6252, 2017. 3
- [70] Zachary Teed and Jia Deng. Raft: Recurrent all-pairs field transforms for optical flow. In *Computer Vision—ECCV 2020: 16th European Conference, Glasgow, UK, August 23–28, 2020, Proceedings, Part II 16*, pages 402–419. Springer, 2020. 3
- [71] Zachary Teed and Jia Deng. Droid-slam: Deep visual slam for monocular, stereo, and rgb-d cameras. *Advances in neural information processing systems*, 34:16558–16569, 2021. 3
- [72] Zhi Tian, Chunhua Shen, Hao Chen, and Tong He. Fcos: Fully convolutional one-stage object detection. In *Proceedings of the IEEE/CVF international conference on computer vision*, pages 9627–9636, 2019. 1
- [73] Bill Triggs, Philip F McLauchlan, Richard I Hartley, and Andrew W Fitzgibbon. Bundle adjustment—a modern synthesis. In *Vision Algorithms: Theory and Practice: International Workshop on Vision Algorithms*, pages 298–372. Springer, 2000. 1
- [74] Yanghai Tsin and Takeo Kanade. A correlation-based approach to robust point set registration. In *Proc. European Conf. Comput. Vis.*, pages 558–569. Springer Berlin Heidelberg, 2004. 3, 4
- [75] Greg Turk. The stanford 3d scanning repository, 2000. URL <https://graphics.stanford.edu/data/3Dscanrep/>. 2, 6, 7, 8, 9, 10
- [76] Tommi Tykkälä and Andrew I Comport. A dense structure model for image based stereo slam. In *Proc. IEEE Int. Conf. Robot. and Automation*, pages 1758–1763. IEEE, 2011. 5
- [77] Fei Wang, Baba C Vemuri, Anand Rangarajan, and Stephan J Eisenschenk. Simultaneous nonrigid registration of multiple point sets and atlas construction. *IEEE Trans. Pattern Anal. Mach. Intell.*, 30(11):2011–2022, 2008. 2
- [78] Rui Wang, Martin Schworer, and Daniel Cremers. Stereo dso: Large-scale direct sparse visual odometry with stereo cameras. In *Proceedings of the IEEE International Conference on Computer Vision*, pages 3903–3911, 2017. 9
- [79] Wenshan Wang, DeLong Zhu, Xiangwei Wang, Yaoyu Hu, Yuheng Qiu, Chen Wang, Yafei Hu, Ashish Kapoor, and Sebastian Scherer. Tartanair: A dataset to push the limits of visual slam. In *Proc. IEEE/RSJ Int. Conf. Intell. Robots and Syst.*, pages 4909–4916. IEEE, 2020. 2, 7, 8, 9, 10, 11
- [80] Thomas Whelan, Hordur Johannsson, Michael Kaess, John J Leonard, and John McDonald. Robust real-time visual odometry for dense rgb-d mapping. In *2013 IEEE International Conference on Robotics and Automation*, pages 5724–5731. IEEE, 2013. 2
- [81] Thomas Whelan, Renato F Salas-Moreno, Ben Glocker, Andrew J Davison, and Stefan Leutenegger. Elasticfusion: Real-time dense slam and light source estimation. *Int. J. Robot. Res.*, 35(14):1697–1716, 2016. 1, 2, 3, 9, 11
- [82] Fang Wu and Giovanni Beltrame. Direct sparse odometry with planes. *IEEE Robotics and Automation Letters*, pages 1–1, 2021. doi: 10.1109/LRA.2021.3130648. 1
- [83] Jiatian Wu. Direct Sparse Odometry with Stereo Cameras, January 2023. URL <https://github.com/JiatianWu/stereo-dso>. original-date: 2017-02-23T07:49:13Z. 9, 11
- [84] Haofei Xu, Jing Zhang, Jianfei Cai, Hamid Rezaatofghi, Fisher Yu, Dacheng Tao, and Andreas Geiger. Unifying flow, stereo and depth estimation. *arXiv preprint arXiv:2211.05783*, 2022. 9
- [85] Heng Yang, Jingnan Shi, and Luca Carlone. Teaser: Fast and certifiable point cloud registration. *IEEE Transactions on Robotics*, 37(2):314–333, 2020. 6
- [86] Nan Yang, Rui Wang, Jorg Stuckler, and Daniel Cremers. Deep virtual stereo odometry: Leveraging deep depth prediction for monocular direct sparse odometry. In *Proceedings of the European conference on computer vision (ECCV)*, pages 817–833, 2018. 3
- [87] Nan Yang, Lukas von Stumberg, Rui Wang, and Daniel Cremers. D3vo: Deep depth, deep pose and deep uncertainty for monocular visual odometry. In *Proceedings of the IEEE/CVF conference on computer vision and pattern recognition*, pages 1281–1292, 2020. 3

- [88] Christopher Zach. Robust bundle adjustment revisited. In *Proc. European Conf. Comput. Vis.*, pages 772–787. Springer, 2014. 5
- [89] Ji Zhang and Sanjiv Singh. Loam: Lidar odometry and mapping in real-time. In *Robotics: Science and systems*, volume 2, pages 1–9. Berkeley, CA, 2014. 3
- [90] Jianbo Zhang, Liang Yuan, Teng Ran, Qing Tao, and Li He. Bayesian nonparametric object association for semantic slam. *IEEE Robotics and Automation Letters*, 6(3):5493–5500, 2021. 3
- [91] Ray Zhang, Tzu-Yuan Lin, Chien-Erh Lin, Steven A. Parkison, William Clark, Jessy W. Grizzle, Ryan M. Eustice, and Maani Ghaffari. A new framework for registration of semantic point clouds from stereo and rgb-d cameras. *Proc. IEEE Int. Conf. Robot. and Automation*, pages 12214–12221, 2020. 2, 3, 4, 5, 6, 9, 11
- [92] Xiaoyu Zhang, Wei Wang, Xianyu Qi, Ziwei Liao, and Ran Wei. Point-plane slam using supposed planes for indoor environments. *Sensors*, 19(17), 2019. ISSN 1424-8220. doi: 10.3390/s19173795. 1
- [93] Qian-Yi Zhou, Jaesik Park, and Vladlen Koltun. Fast global registration. In *Computer Vision–ECCV 2016: 14th European Conference, Amsterdam, The Netherlands, October 11–14, 2016, Proceedings, Part II 14*, pages 766–782. Springer, 2016. 6, 7
- [94] Minghan Zhu, Maani Ghaffari, William A Clark, and Huei Peng. E2pn: Efficient se (3)-equivariant point network. In *Proceedings of the IEEE/CVF Conference on Computer Vision and Pattern Recognition*, pages 1223–1232, 2023. 2, 5
- [95] Jon Zubizarreta, Iker Aguinaga, and Jose Maria Martinez Montiel. Direct sparse mapping. *IEEE Trans. Robot.*, 36(4):1363–1370, 2020. 1